Chemical Science

ROYAL SOCIETY OF CHEMISTRY

EDGE ARTICLE

View Article Online
View Journal | View Issue

Cite this: *Chem. Sci.*, 2025, **16**, 8910

All publication charges for this article have been paid for by the Royal Society of Chemistry

Received 24th January 2025
Accepted 14th April 2025

DOI: 10.1039/d5sc00671f

rsc.li/chemical-science

Intensive near-infrared emitting Au_7Cu_{10} nanoclusters for both energy and electron harvesting†

Wei Zhang, ‡[a] Tingting Xu,‡[b] Jie Kong, ‡[a] Yuanming Li,[a] Xiaoguo Zhou, [a] Jiachen Zhang,[a] Qun Zhang, [a] Yongbo Song, *[b] Yi Luo *[ac] and Meng Zhou *[a]

Triplet excitons have gained increasing recognition as inherent characteristics of various nanomaterials. However, the practical application of triplet excitons is limited due to their confinement within the material where they originate, posing significant challenges to harnessing their potential. In this work, we report direct extraction of both triplet energy and electrons from newly synthesized atomically precise Au_7Cu_{10} nanoclusters (NCs). These NCs exhibit intensive near-infrared (NIR) emission with a quantum yield of 31% at room temperature. They also display near-unity quantum yield of intersystem crossing (ISC) with strong spin–orbit coupling (SOC) up to 864 cm^{-1}. Consequently, Au_7Cu_{10} NCs can act as triplet sensitizers, facilitating efficient triplet–triplet annihilation and achieving upconverted emission with an efficiency of 18.4% in perylene. Furthermore, rapid electron injection from Au_7Cu_{10} NCs in the triplet state to methyl viologen was clearly observed. This study represents the first direct extraction of both triplet energy and electrons from the same metal NCs, indicating their potential as molecular triplet energy and electron surrogates in optoelectronics, photocatalysis, and solar energy conversion.

Introduction

At the forefront of materials science, there is significant interest in the intricate interplay between nanomaterials and organic molecules, particularly in the context of triplet energy transfer (TET) and photoinduced electron transfer (PET).[1–11] Nanomaterial–organic hybrids play a central role in facilitating the precise transfer of triplet excitons and electrons,[12–16] which is fundamental to fields ranging from optoelectronics to photocatalysis.[17–20] The exploration of PET from nanomaterials to organic molecules has emerged as a promising avenue, offering an alternative pathway alongside TET for manipulating triplet exciton utilization.[21–26] Despite significant efforts to understand triplet exciton utilization in quantum nanomaterials, the mechanisms for directly extracting triplet energy and electrons from nanomaterials remain elusive.

The advent of atomically precise metal nanoclusters (NCs) has opened new opportunities for exploring and refining triplet exciton utilization. Metal NCs represent an innovative category of luminescent nanomaterials, which exhibit molecular-like behaviors, characterized by tunable band gaps, unique optical and electronic properties.[27–40] These distinctive attributes can be finely tuned by adjusting parameters such as size, structure, and metal composition, which have found tremendous applications.[41–51] While there have been some instances of PET processes from metal NCs to organic materials,[52–59] these occurrences remain limited. Furthermore, the utilization of metal NCs as a platform for triplet sensitizers was reported recently, particularly in triplet–triplet annihilation-induced upconversion (TTA-UC) emission.[60–64] Therefore, advancing the practical applications of metal NCs requires a deep dive into the mechanisms of electron and energy transfer within these materials, crucial for their development and utilization in triplet sensitizers, optical sensing, and catalysis applications.

To achieve triplet energy and electron extraction from metal NCs, we designed and synthesized a new Au nanocluster alloyed with Cu heteroatoms. This design strategy was based on two key factors: (1) the introduction of Cu atoms could enhance the PLQY;[30] (2) heteroatom doping is an effective strategy to engineer and enrich the electronic structures, potentially yielding unique physicochemical properties and functionalities.[46,60,65] Here, we report the direct extraction of both triplet energy and

[a]*Hefei National Research Center for Physical Sciences at the Microscale, Department of Chemical Physics, University of Science and Technology of China, Hefei, Anhui 230026, China. E-mail: mzhou88@ustc.edu.cn; yiluo@ustc.edu.cn*

[b]*School of Biomedical Engineering, Research and Engineering Center of Biomedical Materials, Anhui Medical University, Hefei, Anhui 230032, China. E-mail: ybsong860@ahmu.edu.cn*

[c]*Hefei National Laboratory, University of Science and Technology of China, Hefei, Anhui 230088, China*

† Electronic supplementary information (ESI) available: Materials and methods, supplementary text, Fig. S1–S15, and Table S1. CCDC 2350273. For ESI and crystallographic data in CIF or other electronic format see DOI: https://doi.org/10.1039/d5sc00671f

‡ These authors contributed equally to this work.

electrons from atomically precise Au_7Cu_{10} NCs that exhibit intense NIR emission. The crystal structure of Au_7Cu_{10}, elucidated through single-crystal X-ray diffraction (SC-XRD), reveals an icosahedral core comprising seven Au atoms and six Cu atoms, with an additional four Cu atoms forming the cap. The PL quantum yield (PLQY) of Au_7Cu_{10} NCs reaches 31% in deaerated solution and 24% in oxygen saturated solutions. Theoretical calculations confirm the presence of strong spin–orbit coupling (SOC) and a minimal energy gap (25 meV) between S_1 and T_2/T_3 states, accelerating the intersystem crossing (<0.1 ps) process. Significant TET from Au_7Cu_{10} to perylene (Pery for short) was observed, confirming the phosphorescent nature of the PL from Au_7Cu_{10}, and the triplet state lifetime is up to 3.9 μs. Additionally, the Au_7Cu_{10} NCs act as efficient triplet energy donors, facilitating upconverted emission of Pery through efficient triplet–triplet annihilation (TTA) with an impressive efficiency of up to 18.4%. Furthermore, femtosecond transient absorption spectroscopy (fs-TA) captures the rapid PET process within 12 picoseconds between Au_7Cu_{10} NCs and methyl viologen. The successful extraction of triplet energy and electrons from Au_7Cu_{10} can be attributed to its unique structure featuring a significant number of exposed metal atoms, which eliminates the shielding effect and promotes efficient energy and electron exchange between the metal NCs and energy/electron acceptors.

Results and discussion

Crystal structure and steady state optical properties

Details of the synthesis of Au_7Cu_{10} NCs are provided in the ESI.† The structure in Fig. 1A reveals a core composition of the Au_7Cu_{10} kernel, which comprises an Au_7Cu_6 icosahedron that is capped by one up-Cu atom and three down-Cu atoms. Within the Au_7Cu_6 icosahedron, the average Au_{core}–M_{shell} and M_{shell}–M_{shell} (M = Au or Cu) distances measure 2.663 Å and 2.857 Å, respectively, which are notably shorter than those observed in an Au_{13} icosahedron (2.757 and 2.908 Å),[66] indicating that Cu-doping induces a contraction in the entire icosahedron. Regarding surface-protecting ligands, the Au_7Cu_{10} kernel is co-capped by three 1-adamantanethiol (1-Adm), six disphenyl-2-pyridylphosphine (Ph_2PyP), and three Cl atoms through Cu–N/S and Au–Cl/P coordination (Fig. 1A). The incorporation of Cu–N enhances the structural rigidity, thereby facilitating the improvement of its luminescence efficiency.[30] Furthermore, the presence of three $[SbF_6]^-$ ions around the entire Au_7Cu_{10} nanocluster suggests a 3+ charge for this nanocluster. Consequently, the precise chemical formula of this nanocluster is expressed as $[Au_7Cu_{10}(1\text{-Adm})_3(PPh_2Py)_6Cl_3](SbF_6)_3$, abbreviated as Au_7Cu_{10}. Besides, the chemical composition of Au_7Cu_{10} was also testified by electrospray ionization mass spectrometry (ESI-MS). As shown in Fig. 1B, a main peak at 1400.257 Da was observed, which can be assigned to $[Au_7Cu_{10}(1\text{-Adm})_3(PPh_2Py)_6Cl_3]^{3+}$ (cal. m/z = 1400.250 Da). The experimental isotopic pattern (red line) is in good agreement with the simulated one (black line).

The steady-state electronic characteristics of Au_7Cu_{10} NCs were explored using the absorption and PL spectra (Fig. 1C) in THF. The absorption spectrum of Au_7Cu_{10} NCs shows distinctive peaks centered at 365 nm and 635 nm. Notably, Au_7Cu_{10} NCs exhibit a pronounced emission band at 740 nm in solution, with a high PLQY of 26% in air. It is observed that only one single peak is observed in the PL spectrum (Fig. 1C) of Au_7Cu_{10} and the time-resolved PL measurements exhibit a long lifetime of 3.5 μs in air (Fig. 1D). To further reveal the emission characteristics, the time-resolved PL decay curves at short-

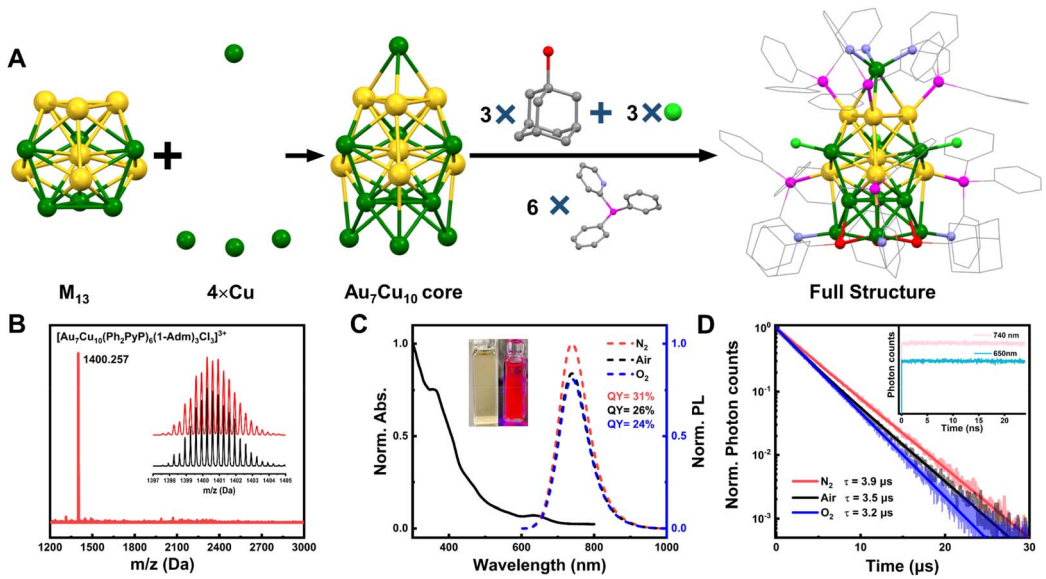

Fig. 1 (A) Crystal structures of Au_7Cu_{10}. Color codes: yellow, Au; green, Cu; magenta, P; light green, Cl; red, S; gray, C; purple, N. (B) ESI-MS of Au_7Cu_{10}. (C) The UV-vis absorption spectrum (solid line) and emission spectra (dashed lines) of Au_7Cu_{10} in diluted THF solution. The inset shows the cluster solution picture without and with UV excitation. (D) Emission decay curves (2.5 ns bin time and probe 740 nm) of Au_7Cu_{10} measured under N_2-degassed, air-saturated and O_2-saturated conditions (λ_{ex} = 375 nm), respectively. The inset shows the PL decay profiles measured with a bin time of 25 ps (monitored at $\lambda_{em} \sim 650$ nm and $\lambda_{em} \sim 740$ nm).

wavelength and long-wavelength of the emission band were examined, wherein we confirmed that there is only one emission component across the entire emission band because all the PL decay curves remain the same on different time scales. Additionally, PL excitation spectra at different emission wavelengths (Fig. S1†) closely resemble the absorption spectrum, providing further evidence that Au_7Cu_{10} possesses only one luminescent excited state.

To discern the intricate details governing the emission behavior of Au_7Cu_{10}, a comprehensive investigation involving PLQY and lifetime measurements was performed under varied atmospheric conditions – oxygen (O_2), air, and nitrogen (N_2) environments. The PLQY of Au_7Cu_{10} exhibits a reduction of 16% in air (QY = 26%) compared to that in N_2 (QY = 31%, see Fig. 1C). In addition, the PLQY exhibits a relatively minor decrease of only 8% when exposed to O_2 as opposed to air (Fig. 1C). Concomitant PL lifetime measurements were conducted, yielding values of 3.9 μs, 3.5 μs, and 3.2 μs in N_2, air, and O_2 atmospheres (Fig. 1C), respectively. These findings underscore that the emission of Au_7Cu_{10} remains largely unaffected by the presence of O_2. It is crucial to note that the absence of PL quenching by O_2, indicative of no discernible formation of singlet oxygen ($^1O_2^*$), does not conclusively establish fluorescence as the primary emission mechanism of Au_7Cu_{10} NCs. The low solubility and slow diffusion rate of O_2 in organic solvents, the degree of ligand shielding of the metal core, and inefficient charge transfer or energy exchange between the metal NCs and O_2 could potentially impede the triplet energy transfer to O_2.[63] The existence of a microsecond lifetime for Au_7Cu_{10} in the O_2 atmosphere further supports the notion that the PL is not completely quenched. Additionally, the PL decay curves at 650 nm and 740 nm in the nanosecond regime were collected, as illustrated in the inset of Fig. 1D, which further demonstrates a single emissive excited state.

Triplet energy transfer

Direct triplet–triplet energy transfer is an effective route to utilize the triplet exciton for solar-associated applications. Fig. 2A illustrates the schematic diagram of the photon upconversion mechanism based on TTA. Pery was chosen as an appropriate triplet annihilator and blue-light emitter, leveraging its high fluorescence quantum yield and the strategic positioning of its lowest-lying triplet energy level at 1.53 eV.[67,68] Notably, the energy gap of T_1 energy levels between Au_7Cu_{10} NCs (Table 1) and Pery is less than 0.15 eV (1.67–1.53 = 0.14 eV), which can reduce the energy loss during TET from the NCs to the Pery molecules.

Upon the introduction of Pery, the absorbance and spectral shape of the absorption band at 600–700 nm for Au_7Cu_{10} undergo minimal changes (Fig. 2B). This observation rules out the formation of complexes between Au_7Cu_{10} and Pery, suggesting that Au_7Cu_{10} NCs maintain their size and composition in the presence of Pery. A gradual decrease in the PL intensity of Au_7Cu_{10} NCs was observed with the increment of the Pery concentration, as depicted in Fig. 2C. A maximum quenching of approximately 94% was observed with the addition of 6.6 mM Pery. It should be noted that the addition of Pery didn't change the entire PL profile even with a Pery concentration of 6.6 mM. The Föster energy transfer and inner filter effect mechanisms that may cause the PL suppression can be safely ruled out because Pery does not display any appreciable absorption at the photoexcitation and photoemission wavelengths of Au_7Cu_{10} (Fig. S2†). Therefore, we can conclude that the TET reaction occurs between Au_7Cu_{10} and Pery as a result of Dexter energy

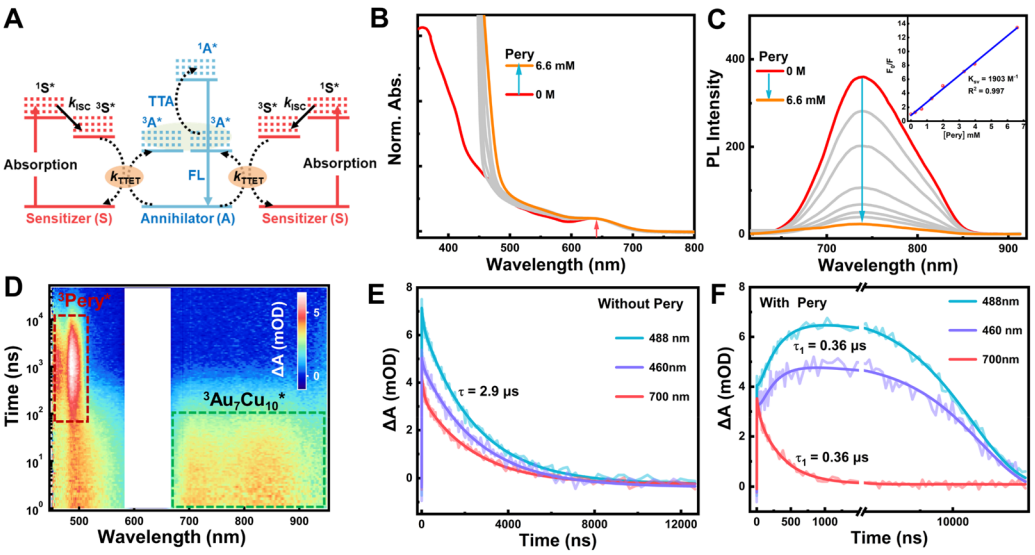

Fig. 2 (A) Schematic energy-level diagram of TTA-UC. Steady-state (B) absorption and (C) emission spectra (excitation at 600 nm) of Au_7Cu_{10} NCs in the presence of Pery. The inset of (C) shows the Stern–Volmer plot with the dynamic quenching rate constant K_{SV}. (D) Ns-TA color maps of Au_7Cu_{10}/Pery dissolved in deaerated THF with 630 nm excitation; the Pery concentration was set at 3 mM. (E) The kinetic traces of Au_7Cu_{10} in THF. (F) The kinetic traces of Au_7Cu_{10}/Pery in THF with 630 nm excitation.

Table 1 Photophysical parameters of Au_7Cu_{10} in THF

Sensitizer	τ^a/μs	$E_{edge}{}^b$/eV (nm)	$E_T{}^c$/eV (nm)	$\Phi_{ISC}{}^d$	$k_{ISC}{}^d/10^{12}$ s^{-1}	$\Phi_P{}^e$
Au_7Cu_{10}	3.9	1.77 (700)	1.67 (740)	1	>10	0.31

[a] Obtained from the PL lifetime *via* the PL decay profiles as shown in Fig. 1D. [b] Absorption edge energy. [c] T_1 energy level (E_T) is evaluated using the photoluminescence peak. [d] ISC quantum yield and the ISC rate constant for Au_7Cu_{10} are obtained from the fs-TA experiment. [e] Absolute PLQY in solution with saturated N_2.

transfer. Based on the TET results, the PL in Au_7Cu_{10} can be safely assigned to phosphorescence.

To quantify the effective TET between Au_7Cu_{10} NCs and Pery, we analyzed PL quenching data using the Stern–Volmer equation, $F_0/F = 1 + K_{sv}[Pery]$,[60,61] where F_0 and F represent the fluorescence intensities before and after the addition of Pery, respectively, K_{sv} is the quenching constant. The resultant Stern–Volmer plot, characterized by a linear dependence (inset of Fig. 2C), signifies a typical hallmark of dynamic quenching. This implies that diffusion predominantly governs the PL quenching processes, with a determined Stern–Volmer constant of 1903 M^{-1}. Besides, the observed decrease in the PL lifetime (from 3.9 to 0.3 μs) of Au_7Cu_{10} upon interaction with Pery, as depicted in Fig. S3,† stems from the quenching of the luminescent state *via* the TET process. Based on the relation of $k_{TET} = K_{sv}/\tau_0$,[60] the corresponding k_{TET} in the presence of Au_7Cu_{10} NCs and Pery was calculated to be 4.8×10^8 M^{-1} s^{-1}, showing an efficient TET process.

To unravel the origin of Au_7Cu_{10} PL and confirm the efficient energy transfer with Pery, a time-resolved spectroscopic investigation of PL quenching was conducted. Fig. 2D and S4A† present the ns-TA spectra of the Au_7Cu_{10} NCs in the presence and absence of Pery, respectively. The ns-TA spectra (Fig. S4A and B†) show the excited-state absorption (ESA) with a maximum at 500 nm and another band with several features extending over the range of 670–950 nm. The ground-state bleaching (GSB) at 630 nm is not observable due to overlapping with the excitation beam. The fitting of TA kinetic traces at different wavelengths for pure Au_7Cu_{10} NCs reveals time constants of 2.9 μs (Fig. 2E). It is observed that the lifetime obtained from ns-TA is slightly shorter than that from PL decay profiles (Fig. 1D). This slight difference is attributed to the fact that the two lifetimes were measured using different instruments, each with distinct instrument response functions and detection limits, leading to the small variation in the observed lifetimes. By comparing the ns-TA kinetic traces of Au_7Cu_{10} NCs before and after the addition of Pery (Fig. 2F), we found that the decay of ESA bands between 700 and 900 nm is much accelerated with Pery addition. Besides, two new ESA bands appear at 450–500 nm (Fig. 2D), which can be assigned to the triplet–triplet absorption of Pery. The rise time (≈0.36 μs, Fig. 2F) of the triplet signal of Pery matches well with the decay time of the ESA bands of the Au_7Cu_{10} NCs (0.36 μs), indicating that the triplet state of Pery (^{3}Pery*) was solely generated *via* TET from the Au_7Cu_{10} NCs. The triplet signal of ^{3}Pery* in Fig. 2D, in accordance with previous reports,[69–71] further confirms the accuracy of the assignment. Global analysis (Fig. S4D†) suggests a two-species model as the best fit for the data, and the first component can be assigned to the TET process.

Using the obtained triplet lifetime from ns-TA, the TET quantum efficiency (Φ_{TET}) was calculated according to $\Phi_{TET} = 1 - \tau/\tau_0$, where τ_0 and τ represent the triplet lifetime of Au_7Cu_{10} in the absence and presence of Pery, respectively. A satisfactory Φ_{TET} value approaching 90% was achieved. The kinetic trace (Fig. S5†) further confirms that the TET rate increases significantly with an increase in the Pery concentration, which supports the conclusion of diffusion-controlled energy transfer. The k_{TET} value (4.8×10^8 M^{-1} s^{-1}) is two orders of magnitude smaller than the estimated diffusion-limited rate constant (k_d) of ~1.51×10^{10} M^{-1} s^{-1} (see the ESI†). This is because the rate constant for Dexter-type energy transfer decays exponentially with the distance between the donor and acceptor. As illustrated in Fig. S6,† the spin density distribution of the lowest triplet state of Au_7Cu_{10} is mainly localized on the metal core rather than the surface ligand moieties, which sterically inhibits the electron exchange between Au_7Cu_{10} and Pery and thus reduces the TET rate.

Ultrafast intersystem crossing

To thoroughly understand the excited state relaxation mechanism of Au_7Cu_{10} NCs, we focused on the ISC process from singlet to triplet states by employing time-resolved fs-TA experiments and theoretical calculations. Fs-TA data maps of Au_7Cu_{10} in THF obtained upon 360 nm excitation are presented in Fig. S7B.† The initial TA spectrum displays two ESA peaks at ~500 and ~590 nm, along with a broad ESA band at ~700–770 nm. Notably, the ESA bands at 590 and 685 nm rapidly disappear within the first picosecond (~360 fs), accompanied by the rapid decay at 685 nm and the generation at 750 nm (Fig. 3A), while the remaining characteristic peaks persist for up to ~10 μs (Fig. S7A and E†). These long-lived ESA bands are assigned to the T_1 state.

Further assignment of the sub-picosecond (~360 fs) component observed in Au_7Cu_{10} with 360 nm excitation was conducted by ultrafast spectroscopy with a long-wavelength (λ = 630 nm) excitation (Fig. S7D†), revealing only a long-lived component with the absence of the sub-picosecond component. A comparison of fs-TA with excitation at 360 nm and 630 nm (Fig. 3B) suggests that the pure ISC process of Au_7Cu_{10} is too fast to be resolved using the current TA spectrometer (IRF = 100 fs). The 360 fs process is then attributed to the internal conversion coupled ISC process. Therefore, it can be deduced that the k_{ISC} is much faster compared to k_{fluor} so that fluorescence is completely suppressed, which indicates an almost

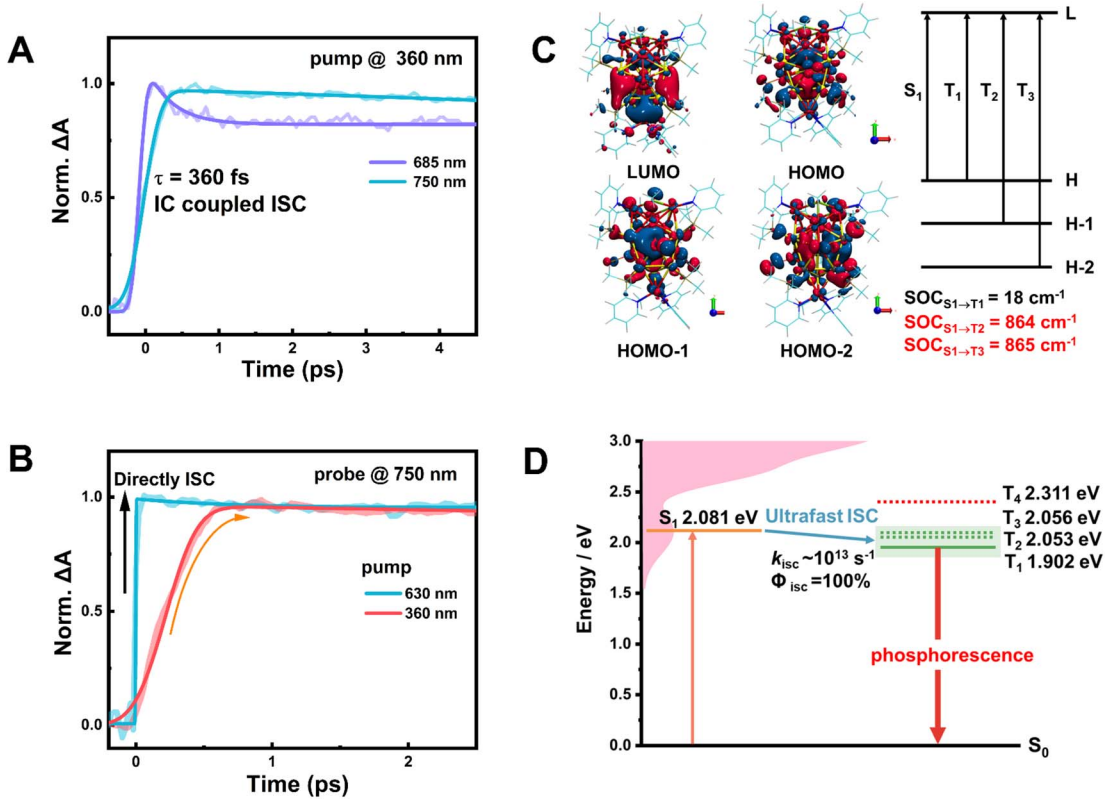

Fig. 3 (A) Fs-TA kinetic traces and fittings at selected probe wavelengths pumped at 360 nm. (B) Comparison of the TA kinetic trace of 750 nm at different excitation wavelengths of 360 and 600 nm. (C) Molecular orbitals corresponding to the hole and electron distributions of the S_1 and T_{1-3} states. SOC values between S_1 and T_n are shown. (D) Simplified energy diagram showing the ultrafast ISC processes of Au_7Cu_{10}. The low-lying excited states energy level values are derived from TD-DFT. ISC: intersystem crossing; IC: internal conversion.

unity ISC yield. A near unity ISC yield makes Au_7Cu_{10} an ideal triplet sensitizer for TTA-UC.

To delve into a comprehensive understanding of the near unity ISC yield of Au_7Cu_{10}, an analysis of decisive factors determining the ISC was carried out through density functional theory (DFT) and time-dependent-DFT (TD-DFT) calculations (Fig. S8†). According to El-Sayed's rules,[72] an efficient ISC is characterized by the simultaneous presence of strong spin–orbit coupling and a small singlet–triplet energy gap of different character states. Electronic structure calculations predict sizable spin–orbit coupling (SOC) values between S_1 and T_2/T_3 states ($\geq$860 cm^{-1}, very large) for Au_7Cu_{10} (Fig. 3C). Beside the intensive SOC, these two triplet states present small vertical energy gaps with respect to S_1 (only 25–28 meV), hence providing the necessary ingredients for efficient ISC. Moreover, the electron/hole pair densities for the S_1 and T_{1-3} states of Au_7Cu_{10} (Fig. 3C and S9†) show that the electrons of T_{1-3} and S_1 are almost the same, mainly delocalized on the surface of the metal core. We noted that the ligands show minimal impact on the molecular orbital isosurface of Au_7Cu_{10} as shown in Fig. 3C. The electron, hole, and charge density difference (CDD) analyses in Fig. S9† further support this observation. Since the investigation of ISC pathways is the primary focus of this work, we have not extensively discussed ligand-associated charge transfer.

As illustrated in Fig. S9,† the CDD indicate a charge transfer character, clearly demarcating the boundary between "electrons" and "holes" in these states. Specifically, the hole distribution in the T_1 state closely resembles that in the S_1 state, whereas the hole distributions in T_2 and T_3 states are perpendicular to that in S_1, respectively. This alteration in orbital angular momentum associated with a 90° rotation can trigger effective SOCs and rapid ISC between S_1 and T_2/T_3, as it can compensate for the change in the spin angular momentum associated with ISC. Consequently, these calculations indicate that the ultrafast ISC process from S_1 to the T_2/T_3 represents the most probable ISC pathways (Fig. 3D), owing to the relatively small ΔE_{ST} energy gaps and substantial SOC values. Moreover, these triplet states exhibit distinct spatial localization relative to the relaxed S_1 state (Fig. 3C and S9†). The presence of metal atoms, along with a non-zero overlap in singlet–triplet wave functions, engenders a robust SOC, facilitating efficient singlet-to-triplet ISC in Au_7Cu_{10}. Meeting all El-Sayed's criteria, Au_7Cu_{10} undergoes an ultrafast spin-flip process driven by inherently strong spin–orbit coupling, complemented by a small ΔE_{ST}.

TTA-UC performance

The broad absorption in the visible region, coupled with efficient ISC and a long-lived triplet excited state, positions Au_7Cu_{10} as a promising candidate for triplet photosensitizers in TTA-UC.

To validate this potential, TTA-UC experiments were conducted on Au_7Cu_{10} dissolved in deaerated THF, employing Pery as the annihilator and blue emitter (Fig. 4). Upon excitation at 663 nm, triplet Au_7Cu_{10} NCs efficiently sensitize $^3Pery^*$ with a noteworthy anti-Stokes shift exceeding 0.88 eV (Fig. 4A). Relative to other NIR to visible UC systems, the anti-Stokes shift of 0.88 eV observed in this work represents an effective UC performance.[73,74] The intensity of upconverted fluorescence progressively increases with increasing Pery concentration, saturating when the concentration exceeds 2.5 mM. The highest upconversion quantum yield is estimated to be 18.4% at a Pery concentration of 2.5 mM (the Φ_{UC} calculation can be found in the ESI and Fig. S10†). It's worth mentioning that a decline in quantum yield is observed with further increments in the Pery concentration, attributed to the formation of Pery excimers, as reported previously.[75,76] Besides, compared to the previously reported Au_4Cu_4-DPA (9,10-diphenylanthracene) system,[60] which achieved an upconversion quantum yield of 28%, higher than the efficiency in our work, several factors could account for this difference: (1) the triplet energy gap between Au_4Cu_4 and DPA is near zero, whereas for Au_7Cu_{10} and Pery it is approximately 0.14 eV. (2) The DPA concentration in the previous study was 40 mM, significantly higher than the 2.5 mM concentration of Pery used in our study. (3) The excited-state lifetime of Au_4Cu_4 was 7.9 μs, longer than the 3.9 μs lifetime of Au_7Cu_{10}, and a longer excited-state lifetime allows more excited nanoclusters to participate in TET with organic acceptors (note that both lifetimes were obtained from photoluminescence decay curves in degassed THF).

Furthermore, the upconversion emission spectral intensity demonstrates a direct correlation with the excitation power density. Fig. 4C shows the integrated upconversion emission intensity of Pery within the 450 to 600 nm range as a function of the laser power density. The integrated upconversion emission intensity of Pery from 450 to 600 nm exhibits a quadratic-to-linear dependence on the laser power density (Fig. 4D), indicating typical behavior observed in TTA-UC systems. Specifically, the slope of the linear fit changes prominently from 2.1 (77 to 2000 mW cm^{-2}) to 1.08 (2290 to 5200 mW cm^{-2}), showcasing an approximate threshold excitation intensity (I_{th}) value of approximately 2065 mW cm^{-2}. In TTA-UC systems, the quadratic-to-linear dependence is a distinctive signature of two-photon-induced upconversion luminescence, signifying the TTA-UC process. Additionally, we observe a millisecond time-scale photoluminescence lifetime of Pery in the mixed solution with Au_7Cu_{10} nanoclusters (inset of Fig. 4D), significantly longer than the fluorescence lifetime of pure Pery (Fig. S11†). Such long delayed fluorescence behavior signifies that the observed emission stems from the long-lived TTA process of the emitter molecules, suggesting that the NIR emission from Au_7Cu_{10} can be successfully upconverted to the blue emission of Pery through efficient TET induced upconversion.

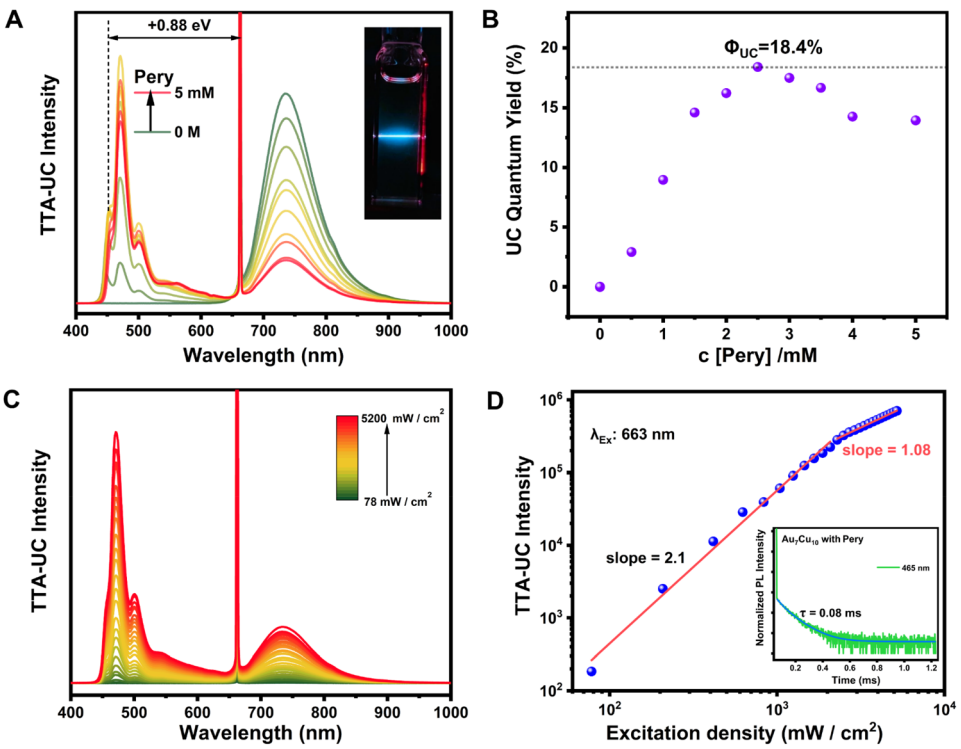

Fig. 4 (A) PL spectra of Au_7Cu_{10} and Pery at various concentrations with excitation at 663 nm, where the inset shows the photograph of the TTA-UC emission process. (B) Relationship of the TTA-UC quantum yield with the Pery concentration. Note that the theoretical maximum of Φ_{UC} is defined as 100%.[73] (C) Dependence of the TTA-UC fluorescence intensity on the excitation power density. (D) Double logarithmic plot of the integrated TTA-UC fluorescence intensity with the excitation power density, where the inset shows the lifetime measurement of delayed fluorescence of Pery.

Photoinduced electron transfer

Au–Cu alloyed nanoclusters have been well known for their wealth of rich redox chemistry in addition to photophysical properties.[60,77,78] Since doping heteroatoms into gold nanoclusters can modulate the energy level scheme and excited state properties, it is reasonable to expect that Au_7Cu_{10} would engage in the PET process. In the context of metal nanoclusters, most research has focused on the triplet energy aspects, neglecting the importance of electrons. Electrochemical measurements (Fig. S12†) indicate that Au_7Cu_{10} can effectively participate in both donating and accepting electrons, demonstrating its capability of acting as an intermediate in the electron transfer process. In addition, the rapid ISC process and long-lived triplet state lifetime of Au_7Cu_{10} provide ample time for electron transfer processes to occur in the triplet state. Such a PET is essential for converting light energy into chemical energy, including applications in dye-sensitized solar cells, organic photovoltaics, artificial photosynthesis, *etc.*[79–81]

Methyl viologen (MV^{2+}), with strong electron-accepting properties and suitable oxidation potential in methanol (MeOH), was employed to probe the excited-state intermolecular electron-transfer between Au_7Cu_{10} (Fig. 5A). Furthermore, MV^{2+} can engage in noncovalent interactions with counter ions on the surface of Au_7Cu_{10} nanoclusters *via* coulombic attraction, enhancing the feasibility of subsequent PET processes. Fig. 5B illustrates the steady state absorption and emission spectra of Au_7Cu_{10} NCs with varying concentrations of MV^{2+}. The absorption band of Au_7Cu_{10} located at 630 nm remains unchanged upon MV^{2+} addition, providing clear evidence of no ground-state interaction between the two components. Concurrently, the emission intensity of Au_7Cu_{10} NCs decreases with an increasing MV^{2+} concentration (Fig. 5C), with over 90% fluorescence intensity quenched at 15 mM MV^{2+}. This efficient quenching indicates that the excited-state deactivation occurs through the PET pathway. The absorption spectra of MV^{2+} show no spectral overlap with Au_7Cu_{10} nanocluster emission, ruling out Förster resonance energy transfer from Au_7Cu_{10} to MV^{2+}.

We then employed the Stern–Volmer relationship to analyze the PL quenching process (inset of Fig. 5C), which demonstrates a diffusion-controlled mechanism with a quenching constant (K_{SV}) of 689 M^{-1}. Examining the thermodynamic feasibility of the PET, a negative free energy of −0.98 eV (ΔG_{ET}) is estimated by applying the Rehm–Weller equation (Table S1†), confirming the thermodynamically favorable electron transfer from Au_7Cu_{10} to MV^{2+}. To further clarify the PET mechanism, fs-TA spectroscopy was carried out to investigate the excited-state dynamic processes between the Au_7Cu_{10} and viologen units. It is observed that the initial spectral evolution of Au_7Cu_{10} in the presence of MV^{2+} (Fig. 5D) corresponds to the formation of the triplet signal of Au_7Cu_{10} ($^3Au_7Cu_{10}^*$), closely resembling the fs-TA spectra of pure Au_7Cu_{10} in the initial 1 ps (Fig. S13†), which can be attributed to the rapid internal conversion-coupled ISC process as we discussed above.

Due to the broad ESA of Au_7Cu_{10} in the visible region, it remains challenging to identify the absorption peak of the oxidized $^3Au_7Cu_{10}^*$. Compared to the spectra of pure Au_7Cu_{10}, new ESA emerges at approximately 600 nm within about 30 picoseconds (Fig. 5D), which is attributed to the reduction of $MV^{+\bullet}$ by Au_7Cu_{10} NCs. The kinetic trace monitored at 700 nm reveals an additional decay (~12 ps, Fig. 5E) which is not observed in pure Au_7Cu_{10}. Simultaneously, a distinct raised signal from the reduced methyl viologen radical ($MV^{+\bullet}$) is evident with absorption maxima around 600 nm (Fig. 5D and E).[55] However, the triplet signal of pure Au_7Cu_{10} persists even at

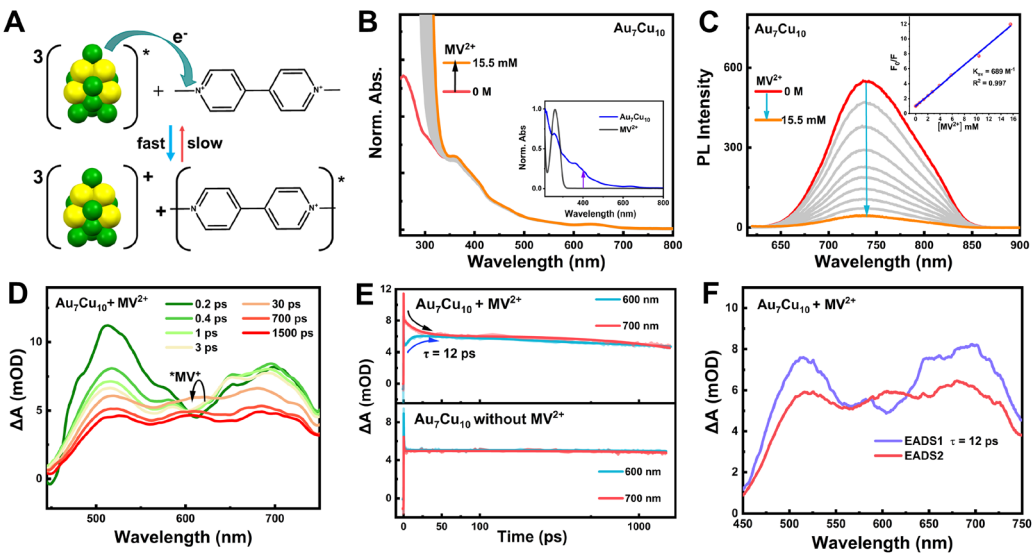

Fig. 5 (A) Schematic illustration of PET between excited Au_7Cu_{10} and MV^{2+}. Steady-state (B) absorption and (C) emission spectra (excitation at 600 nm) of Au_7Cu_{10} NCs in the presence of MV^{2+}. The inset of (B) shows the absorption spectra of Au_7Cu_{10} and MV^{2+} in MeOH. The inset of (C) shows a Stern–Volmer plot. (D) fs-TA of Au_7Cu_{10} NCs in deaerated MeOH after 400 nm laser excitation in the presence of MV^{2+}. (E) Top: TA kinetic traces after laser excitation at 400 nm of Au_7Cu_{10} NCs in the presence of MV^{2+} collected from fs-TA monitored at 600 nm (absorption of MV^+ radical) and 700 nm (ESA of Au_7Cu_{10}). Below: kinetic traces of Au_7Cu_{10} NCs in the absence of MV^{2+}. (F) Global analysis results derived from fs-TA of Au_7Cu_{10} NCs in the presence of MV^{2+}.

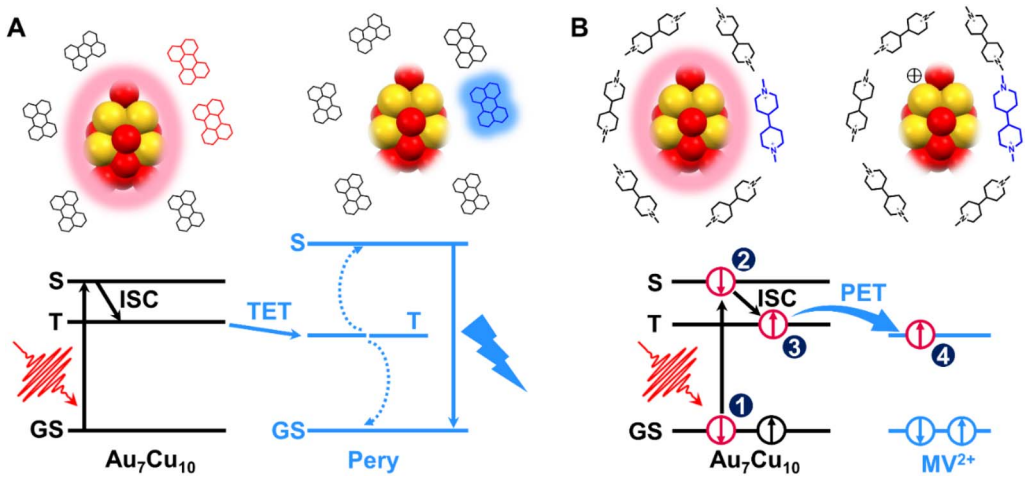

Scheme 1 Schematic diagram of the (A) TET and (B) PET processes between Au_7Cu_{10} NCs and organic acceptors, represented by a single Au_7Cu_{10} NC for simplicity. S: singlet state; T: triplet state; GS: ground state. In the TET process, the NIR emission of Au_7Cu_{10} is quenched as triplet energy is transferred to Pery, resulting in TTA and the subsequent blue fluorescence of Pery. In the PET process, the NIR emission of Au_7Cu_{10} is quenched due to electron transfer from Au_7Cu_{10} to MV^{2+}. The numbers in (B) indicate the sequence of electron motion: (1 → 2) excitation of an electron from the ground state to the singlet state in Au_7Cu_{10} upon photoexcitation, (2 → 3) spin flip *via* ISC from the singlet state to the triplet state, and (3 → 4) PET from Au_7Cu_{10} to MV^{2+}.

longer time delays (Fig. S14C†), indicating an equilibrium process between the triplet state of Au_7Cu_{10} NCs and the PET process. The charge-separated state can undergo back either electron transfer to reform the triplet state or charge recombination to the ground state. Consequently, the fs-TA data of Au_7Cu_{10} in the presence of MV^{2+} can be well reproduced through global fitting using two decay components.

The corresponding evolution-associated difference absorption spectra (EADS) and time constants are depicted in Fig. 5F. It is observed that the first EADS corresponds to the triplet Au_7Cu_{10}. 12 ps later, the second EADS, indicative of the equilibrium state between the triplet state of Au_7Cu_{10} NCs and the PET process, becomes apparent. Besides, noteworthy differences are observed in the ns-TA spectra of the Au_7Cu_{10} NCs in the absence and presence of MV^{2+} (Fig. S14†): (1) the lifetime of triplet Au_7Cu_{10} in the presence of MV^{2+} (370 ns) is much shorter than that in the absence of MV^{2+} (2.8 μs), indicating effective quenching of $^3Au_7Cu_{10}^*$ by MV^{2+}; (2) a distinct band at around 600 nm emerges in the presence of $MV^{+\bullet}$, and the kinetic trace fitting at 600 nm reveals a lifetime of 1.2 μs, which can be assigned to the relaxation to the ground state of $MV^{+\bullet}$. One might wonder why the quenching efficiency of Au_7Cu_{10} by O_2 is low, while its quenching efficiencies by Pery and MV^{2+} are relatively high. As the degree of ligand shielding of the metal core shows similar effects on both O_2 and Pery/MV^{2+} quenching, we tentatively assign the differences to factors including the CT driving force, O_2 solubility, slow diffusion of O_2, and the triplet energy level matching between the donor nanocluster and acceptor O_2, all contributing to the low-efficiency quenching of Au_7Cu_{10} by O_2.

It is essential to clarify that the PET process between Au_7Cu_{10} and MV^{2+} (12 ps^{-1}) is much faster than the TET with the Pery molecule (360 ns^{-1}). This is because TET involves a two-step electron exchange process,[82] while MV^{2+} can be adsorbed on the counterions around the nanocluster, accelerating the one-step PET. In the crystal structure of Au_7Cu_{10}, multiple Cu atoms are exposed to the ambient environment, and the spin density distribution of the triplet state shows that the electrons primarily localize on the copper atoms (Fig. S6†), allowing for efficient TET with suitable molecules and achieving high-efficiency upconversion luminescence. Additionally, our results indicate that both PET and TET can quench the PL of Au_7Cu_{10}. The key distinction between these two mechanisms lies in the nature of the quenching product. PET involves electron transfer, leading to the formation of an anion radical of the organic molecule ($MV^{+\bullet}$), whereas TET involves energy transfer, resulting in the formation of the triplet state of the organic molecule (^{3}Pery*). Compared to previously reported Au_xCu_y nanoclusters,[60] the newly synthesized Au_7Cu_{10} stands out as a dual-function nanocluster capable of serving as both a triplet energy sensitizer and an electron donor (Scheme 1). These advances, supported by extensive experimental and theoretical evidence, position Au_7Cu_{10} as a versatile platform for applications in optoelectronics, photocatalysis, and solar energy conversion. Additionally, directly extracting electrons and the generation of long-lived charge-separated excited states make the systems a potential light-harvesting sensitizer and photo-induced catalyst, opening avenues for numerous applications.[83–85]

Conclusion

In summary, we present the direct extraction of triplet energy from Au_7Cu_{10} NCs through the TET process, inducing triplet–triplet annihilation and upconverted blue fluorescence from Pery. Meanwhile, the PET process enables efficient electron transfer from Au_7Cu_{10} to MV^{2+}, resulting in the formation of an $MV^{+\bullet}$ radical and quenching of the nanocluster's NIR emission.

The crystal structure analysis revealed an icosahedral core of Au_7Cu_6 (M_{13}) surrounded by four Cu atoms in Au_7Cu_{10}. These NCs exhibited a high NIR PLQY exceeding 31% under N_2 conditions at room temperature. Transient spectroscopy of Au_7Cu_{10} unveils the remarkably ultrafast (<1 ps) internal conversion coupled ISC process and a long-lived triplet state (3.5 μs in the air). DFT calculations prove that the strong SOC (864.8 cm^{-1}) significantly promotes ultrafast ISC (<100 fs). Despite the modest quenching influence of O_2 on photoluminescence, the robust TET corroborates the near unity ISC yield, affirming the origin of emission in Au_7Cu_{10} from the triplet state. When combined with the blue light emitter Pery, Au_7Cu_{10} exhibited remarkable upconversion photoluminescence, converting red excitation to blue emission with an efficiency of 18.4%. Additionally, we demonstrated that Au_7Cu_{10} can serve as a light absorber, enabling rapid and efficient electron injection into organic molecules. These findings highlight the tailored design of nanoclusters to facilitate efficient triplet energy and electron transfer, promising advancements in light harvesting and photoenergy conversion applications.

Data availability

Data available on request from the authors.

Author contributions

W. Z. and J. K. performed the spectral measurements and the theoretical calculations. T. X. and Y. S. synthesized and characterized the metal nanoclusters. Y. L. and X. Z. provided help in the measurements of TTA-UC experiments. J. Z and Q. Z. provided help in measuring photoluminescence quantum yield of metal nanoclusters. Y. S., Y. L. and M. Z. designed the project. W. Z., and J. K. wrote the draft. W. Z., J. K., Y. S., Y. L. and M. Z. revised the manuscript. All authors approved the final version of the manuscript.

Conflicts of interest

The authors declare that they have no conflict of interest.

Acknowledgements

We acknowledge the financial support from the Strategic Priority Research Program of the Chinese Academy of Sciences (XDB0450202), the Fundamental Research Funds for the Central Universities (WK9990000145), the National Natural Science Foundation of China (22273095 and 22171007), the Innovation Program for Quantum Science and Technology (2021ZD0303303), and the Chinese Academy of Sciences (YSBR-007).

References

1 C. Mongin, S. Garakyaraghi, N. Razgoniaeva, M. Zamkov and F. N. Castellano, Direct observation of triplet energy transfer from semiconductor nanocrystals, *Science*, 2016, **351**, 369–372.
2 K. Wang, R. P. Cline, J. Schwan, J. M. Strain, S. T. Roberts, L. Mangolini, J. D. Eaves and M. L. Tang, Efficient photon upconversion enabled by strong coupling between silicon quantum dots and anthracene, *Nat. Chem.*, 2023, **15**, 1172–1178.
3 K. Wu and T. Lian, Quantum confined colloidal nanorod heterostructures for solar-to-fuel conversion, *Chem. Soc. Rev.*, 2016, **45**, 3781–3810.
4 C. Nie, X. Lin, G. Zhao and K. Wu, Low-Toxicity ZnSe/ZnS Quantum Dots as Potent Photoreductants and Triplet Sensitizers for Organic Transformations, *Angew. Chem., Int. Ed.*, 2022, **61**, e202213065.
5 X. Luo, Y. Han, Z. Chen, Y. Li, G. Liang, X. Liu, T. Ding, C. Nie, M. Wang, F. N. Castellano and K. Wu, Mechanisms of triplet energy transfer across the inorganic nanocrystal/organic molecule interface, *Nat. Commun.*, 2020, **11**, 28.
6 Z. Huang, Z. Xu, T. Huang, V. Gray, K. Moth-Poulsen, T. Lian and M. L. Tang, Evolution from Tunneling to Hopping Mediated Triplet Energy Transfer from Quantum Dots to Molecules, *J. Am. Chem. Soc.*, 2020, **142**, 17581–17588.
7 N. A. Anderson and T. Lian, Ultrafast Electron Transfer at the Molecule-Semiconductor Nanoparticle Interface, *Annu. Rev. Phys. Chem.*, 2005, **56**, 491–519.
8 B. Shan, T.-T. Li, M. K. Brennaman, A. Nayak, L. Wu and T. J. Meyer, Charge Transfer from Upconverting Nanocrystals to Semiconducting Electrodes: Optimizing Thermodynamic Outputs by Electronic Energy Transfer, *J. Am. Chem. Soc.*, 2019, **141**, 463–471.
9 N. J. Thompson, M. W. B. Wilson, D. N. Congreve, P. R. Brown, J. M. Scherer, T. S. Bischof, M. Wu, N. Geva, M. Welborn, T. V. Voorhis, V. Bulović, M. G. Bawendi and M. A. Baldo, Energy harvesting of non-emissive triplet excitons in tetracene by emissive PbS nanocrystals, *Nat. Mater.*, 2014, **13**, 1039–1043.
10 Y. Peng, B. Lu, F. Wu, F. Zhang, J. E. Lu, X. Kang, Y. Ping and S. Chen, Point of Anchor: Impacts on Interfacial Charge Transfer of Metal Oxide Nanoparticles, *J. Am. Chem. Soc.*, 2018, **140**, 15290–15299.
11 D. M. Cadena, J. K. Sowa, D. E. Cotton, C. D. Wight, C. L. Hoffman, H. R. Wagner, J. T. Boette, E. K. Raulerson, B. L. Iverson, P. J. Rossky and S. T. Roberts, Aggregation of Charge Acceptors on Nanocrystal Surfaces Alters Rates of Photoinduced Electron Transfer, *J. Am. Chem. Soc.*, 2022, **144**, 22676–22688.
12 E. M. Gholizadeh, S. K. K. Prasad, Z. L. Teh, T. Ishwara, S. Norman, A. J. Petty, J. H. Cole, S. Cheong, R. D. Tilley, J. E. Anthony, S. Huang and T. W. Schmidt, Photochemical upconversion of near-infrared light from below the silicon bandgap, *Nat. Photonics*, 2020, **14**, 585–590.
13 S. Han, Z. Yi, J. Zhang, Q. Gu, L. Liang, X. Qin, J. Xu, Y. Wu, H. Xu, A. Rao and X. Liu, Photon upconversion through triplet exciton-mediated energy relay, *Nat. Commun.*, 2021, **12**, 3704.
14 J. T. DuBose and P. V. Kamat, How Pendant Groups Dictate Energy and Electron Transfer in Perovskite–Rhodamine

Light Harvesting Assemblies, *J. Am. Chem. Soc.*, 2023, **145**, 4601–4612.

15 A. Chemmangat, J. Chakkamalayath, J. T. DuBose and P. V. Kamat, Tuning Energy Transfer Pathways in Halide Perovskite–Dye Hybrids through Bandgap Engineering, *J. Am. Chem. Soc.*, 2024, **146**, 3352–3362.

16 T. Huang, S. He, A. Ni, T. Lian and M. Lee Tang, Triplet energy transfer from quantum dots increases Ln(III) photoluminescence, enabling excitation at visible wavelengths, *Chem. Sci.*, 2024, **15**, 4556–4563.

17 W. Liang, C. Nie, J. Du, Y. Han, G. Zhao, F. Yang, G. Liang and K. Wu, Near-infrared photon upconversion and solar synthesis using lead-free nanocrystals, *Nat. Photonics*, 2023, **17**, 346–353.

18 P. Xia, E. K. Raulerson, D. Coleman, C. S. Gerke, L. Mangolini, M. L. Tang and S. T. Roberts, Achieving spin-triplet exciton transfer between silicon and molecular acceptors for photon upconversion, *Nat. Chem.*, 2020, **12**, 137–144.

19 M. La Rosa, S. A. Denisov, G. Jonusauskas, N. D. McClenaghan and A. Credi, Designed Long-Lived Emission from CdSe Quantum Dots through Reversible Electronic Energy Transfer with a Surface-Bound Chromophore, *Angew. Chem., Int. Ed.*, 2018, **57**, 3104–3107.

20 J. Isokuortti, T. Griebenow, J.-S. v. Glasenapp, T. Raeker, M. A. Filatov, T. Laaksonen, R. Herges and N. A. Durandin, Triplet sensitization enables bidirectional isomerization of diazocine with 130 nm redshift in excitation wavelengths, *Chem. Sci.*, 2023, **14**, 9161–9166.

21 X. Luo, G. Liang, Y. Han, Y. Li, T. Ding, S. He, X. Liu and K. Wu, Triplet Energy Transfer from Perovskite Nanocrystals Mediated by Electron Transfer, *J. Am. Chem. Soc.*, 2020, **142**, 11270–11278.

22 S. Wieghold and L. Nienhaus, Precharging Photon Upconversion: Interfacial Interactions in Solution-Processed Perovskite Upconversion Devices, *J. Phys. Chem. Lett.*, 2020, **11**, 601–607.

23 A. M. Steiner, F. Lissel, A. Fery, J. Lauth and M. Scheele, Prospects of Coupled Organic–Inorganic Nanostructures for Charge and Energy Transfer Applications, *Angew. Chem., Int. Ed.*, 2021, **60**, 1152–1175.

24 J. Huang, Z. Huang, Y. Yang, H. Zhu and T. Lian, Multiple Exciton Dissociation in CdSe Quantum Dots by Ultrafast Electron Transfer to Adsorbed Methylene Blue, *J. Am. Chem. Soc.*, 2010, **132**, 4858–4864.

25 H. Zhu, Y. Yang, K. Wu and T. Lian, Charge Transfer Dynamics from Photoexcited Semiconductor Quantum Dots, *Annu. Rev. Phys. Chem.*, 2016, **67**, 259–281.

26 J. T. DuBose and P. V. Kamat, Energy *Versus* Electron Transfer: Managing Excited-State Interactions in Perovskite Nanocrystal–Molecular Hybrids, *Chem. Rev.*, 2022, **122**, 12475–12494.

27 G. Li and R. Jin, Atomically Precise Gold Nanoclusters as New Model Catalysts, *Acc. Chem. Res.*, 2013, **46**, 1749–1758.

28 J. Kong, W. Zhang, Y. Wu and M. Zhou, Optical properties of gold nanoclusters constructed from Au_{13} units, *Aggregate*, 2022, **3**, e207.

29 L. Luo, Z. Liu, J. Kong, C. G. Gianopoulos, I. Coburn, K. Kirschbaum, M. Zhou and R. Jin, Three-atom-wide gold quantum rods with periodic elongation and strongly polarized excitons, *Proc. Natl. Acad. Sci. U. S. A.*, 2024, **121**, e2318537121.

30 W.-Q. Shi, L. Zeng, R.-L. He, X.-S. Han, Z.-J. Guan, M. Zhou and Q.-M. Wang, Near-unity NIR phosphorescent quantum yield from a room-temperature solvated metal nanocluster, *Science*, 2024, **383**, 326–330.

31 Y. Horita, S. Hossain, M. Ishimi, P. Zhao, M. Sera, T. Kawawaki, S. Takano, Y. Niihori, T. Nakamura, T. Tsukuda, M. Ehara and Y. Negishi, Clarifying the Electronic Structure of Anion-Templated Silver Nanoclusters by Optical Absorption Spectroscopy and Theoretical Calculation, *J. Am. Chem. Soc.*, 2023, **145**, 23533–23540.

32 Y. Zhong, J. Zhang, T. Li, W. Xu, Q. Yao, M. Lu, X. Bai, Z. Wu, J. Xie and Y. Zhang, Suppression of kernel vibrations by layer-by-layer ligand engineering boosts photoluminescence efficiency of gold nanoclusters, *Nat. Commun.*, 2023, **14**, 658.

33 S.-S. Zhang, S. Havenridge, C. Zhang, Z. Wang, L. Feng, Z.-Y. Gao, C. M. Aikens, C.-H. Tung and D. Sun, Sulfide Boosting Near-Unity Photoluminescence Quantum Yield of Silver Nanocluster, *J. Am. Chem. Soc.*, 2022, **144**, 18305–18314.

34 X. Zou, X. Kang and M. Zhu, Recent developments in the investigation of driving forces for transforming coinage metal nanoclusters, *Chem. Soc. Rev.*, 2023, **52**, 5892–5967.

35 C. Zhu, J. Xin, J. Li, H. Li, X. Kang, Y. Pei and M. Zhu, Fluorescence or Phosphorescence? The Metallic Composition of the Nanocluster Kernel Does Matter, *Angew. Chem., Int. Ed.*, 2022, **61**, e202205947.

36 Y.-J. Kong, J.-H. Hu, X.-Y. Dong, Y. Si, Z.-Y. Wang, X.-M. Luo, H.-R. Li, Z. Chen, S.-Q. Zang and T. C. W. Mak, Achiral-Core-Metal Change in Isomorphic Enantiomeric $Ag_{12}Ag_{32}$ and $Au_{12}Ag_{32}$ Clusters Triggers Circularly Polarized Phosphorescence, *J. Am. Chem. Soc.*, 2022, **144**, 19739–19747.

37 W. Suzuki, R. Takahata, Y. Chiga, S. Kikkawa, S. Yamazoe, Y. Mizuhata, N. Tokitoh and T. Teranishi, Control over Ligand-Exchange Positions of Thiolate-Protected Gold Nanoclusters Using Steric Repulsion of Protecting Ligands, *J. Am. Chem. Soc.*, 2022, **144**, 12310–12320.

38 Y. Song, Y. Li, M. Zhou, X. Liu, H. Li, H. Wang, Y. Shen, M. Zhu and R. Jin, Ultrabright $Au@Cu_{14}$ nanoclusters: 71.3% phosphorescence quantum yield in non-degassed solution at room temperature, *Sci. Adv.*, 2021, **7**, eabd2091.

39 W. Zhang, J. Kong, Y. Li, Z. Kuang, H. Wang and M. Zhou, Coherent vibrational dynamics of $Au_{144}(SR)_{60}$ nanoclusters, *Chem. Sci.*, 2022, **13**, 8124–8130.

40 Y. Li, G. J. Stec, A. E. Thorarinsdottir, R. D. McGillicuddy, S.-L. Zheng and J. A. Mason, The role of metal accessibility on carbon dioxide electroreduction in atomically precise nanoclusters, *Chem. Sci.*, 2023, **14**, 12283–12291.

41 S. Hossain, D. Hirayama, A. Ikeda, M. Ishimi, S. Funaki, A. Samanta, T. Kawawaki and Y. Negishi, Atomically precise thiolate-protected gold nanoclusters: Current status

of designability of the structure and physicochemical properties, *Aggregate*, 2023, **4**, e255.

42 X. Ouyang, N. Jia, J. Luo, L. Li, J. Xue, H. Bu, G. Xie and Y. Wan, DNA Nanoribbon-Assisted Intracellular Biosynthesis of Fluorescent Gold Nanoclusters for Cancer Cell Imaging, *JACS Au*, 2023, **3**, 2566–2577.

43 Z.-J. Guan, J.-J. Li, F. Hu and Q.-M. Wang, Structural Engineering toward Gold Nanocluster Catalysis, *Angew. Chem., Int. Ed.*, 2022, **61**, e202209725.

44 A. K. Das, S. Biswas, S. S. Manna, B. Pathak and S. Mandal, An atomically precise silver nanocluster for artificial light-harvesting system through supramolecular functionalization, *Chem. Sci.*, 2022, **13**, 8355–8364.

45 S. Zhuang, D. Chen, Q. You, W. Fan, J. Yang and Z. Wu, Thiolated, Reduced Palladium Nanoclusters with Resolved Structures for the Electrocatalytic Reduction of Oxygen, *Angew. Chem., Int. Ed.*, 2022, **61**, e202208751.

46 H. Hirai, S. Takano, T. Nakashima, T. Iwasa, T. Taketsugu and T. Tsukuda, Doping-Mediated Energy-Level Engineering of M@Au_{12} Superatoms (M = Pd, Pt, Rh, Ir) for Efficient Photoluminescence and Photocatalysis, *Angew. Chem., Int. Ed.*, 2022, **61**, e202207290.

47 X. Liu, E. Wang, M. Zhou, Y. Wan, Y. Zhang, H. Liu, Y. Zhao, J. Li, Y. Gao and Y. Zhu, Asymmetrically Doping a Platinum Atom into a Au_{38} Nanocluster for Changing the Electron Configuration and Reactivity in Electrocatalysis, *Angew. Chem., Int. Ed.*, 2022, **61**, e202207685.

48 X. Wang, B. Yin, L. Jiang, C. Yang, Y. Liu, G. Zou, S. Chen and M. Zhu, Ligand-protected metal nanoclusters as low-loss, highly polarized emitters for optical waveguides, *Science*, 2023, **381**, 784–790.

49 W.-D. Si, C. Zhang, M. Zhou, W.-D. Tian, Z. Wang, Q. Hu, K.-P. Song, L. Feng, X.-Q. Huang, Z.-Y. Gao, C.-H. Tung and D. Sun, Two triplet emitting states in one emitter: near-infrared dual-phosphorescent Au_{20} nanocluster, *Sci. Adv.*, 2023, **9**, eadg3587.

50 M. F. Matus and H. Häkkinen, Understanding ligand-protected noble metal nanoclusters at work, *Nat. Rev. Mater.*, 2023, **8**, 372–389.

51 J. Kong, Z. Kuang, W. Zhang, Y. Song, G. Yao, C. Zhang, H. Wang, Y. Luo and M. Zhou, Robust vibrational coherence protected by a core–shell structure in silver nanoclusters, *Chem. Sci.*, 2024, **15**, 6906–6915.

52 W.-T. Chen, Y.-J. Hsu and P. V. Kamat, Realizing Visible Photoactivity of Metal Nanoparticles: Excited-State Behavior and Electron-Transfer Properties of Silver (Ag_8) Clusters, *J. Phys. Chem. Lett.*, 2012, **3**, 2493–2499.

53 S. M. Aly, L. G. AbdulHalim, T. M. D. Besong, G. Soldan, O. M. Bakr and O. F. Mohammed, Ultrafast static and diffusion-controlled electron transfer at Ag_{29} nanocluster/molecular acceptor interfaces, *Nanoscale*, 2016, **8**, 5412–5416.

54 H.-H. Deng, K.-Y. Huang, C.-T. Zhu, J.-F. Shen, X.-P. Zhang, H.-P. Peng, X.-H. Xia and W. Chen, Bell-Shaped Electron Transfer Kinetics in Gold Nanoclusters, *J. Phys. Chem. Lett.*, 2021, **12**, 876–883.

55 K. G. Stamplecoskie and P. V. Kamat, Size-Dependent Excited State Behavior of Glutathione-Capped Gold Clusters and Their Light-Harvesting Capacity, *J. Am. Chem. Soc.*, 2014, **136**, 11093–11099.

56 K. Huang, Q. Fang, W. Sun, S. He, Q. Yao, J. Xie, W. Chen and H. Deng, Cucurbit[n]uril Supramolecular Assemblies-Regulated Charge Transfer for Luminescence Switching of Gold Nanoclusters, *J. Phys. Chem. Lett.*, 2022, **13**, 419–426.

57 A. Domínguez-Castro and T. Frauenheim, Impact of vibronic coupling effects on light-driven charge transfer in pyrene-functionalized middle and large-sized metalloid gold nanoclusters from Ehrenfest dynamics, *Phys. Chem. Chem. Phys.*, 2021, **23**, 17129–17133.

58 K.-Y. Huang, Z.-Q. Yang, M.-R. Yang, T.-S. Chen, S. Tang, W.-M. Sun, Q. Yao, H.-H. Deng, W. Chen and J. Xie, Unraveling a Concerted Proton-Coupled Electron Transfer Pathway in Atomically Precise Gold Nanoclusters, *J. Am. Chem. Soc.*, 2024, **142**(12), 8706–8715.

59 M. Pelton, Y. Tang, O. M. Bakr and F. Stellacci, Long-Lived Charge-Separated States in Ligand-Stabilized Silver Clusters, *J. Am. Chem. Soc.*, 2012, **134**, 11856–11859.

60 D. Arima and M. Mitsui, Structurally Flexible Au–Cu Alloy Nanoclusters Enabling Efficient Triplet Sensitization and Photon Upconversion, *J. Am. Chem. Soc.*, 2023, **145**, 6994–7004.

61 Y. Niihori, Y. Wada and M. Mitsui, Single Platinum Atom Doping to Silver Clusters Enables Near-Infrared-to-Blue Photon Upconversion, *Angew. Chem., Int. Ed.*, 2021, **60**, 2822–2827.

62 M. Mitsui, Y. Wada, R. Kishii, D. Arima and Y. Niihori, Evidence for triplet-state-dominated luminescence in biicosahedral superatomic molecular Au_{25} clusters, *Nanoscale*, 2022, **14**, 7974–7979.

63 M. Mitsui, D. Arima, A. Uchida, K. Yoshida, Y. Arai, K. Kawasaki and Y. Niihori, Charge-Transfer-Mediated Mechanism Dominates Oxygen Quenching of Ligand-Protected Noble-Metal Cluster Photoluminescence, *J. Phys. Chem. Lett.*, 2022, **13**, 9272–9278.

64 K. Yoshida, D. Arima and M. Mitsui, Dissecting the Triplet-State Properties and Intersystem Crossing Mechanism of the Ligand-Protected Au_{13} Superatom, *J. Phys. Chem. Lett.*, 2023, **14**, 10967–10973.

65 R. Jin, C. Zeng, M. Zhou and Y. Chen, Atomically Precise Colloidal Metal Nanoclusters and Nanoparticles: Fundamentals and Opportunities, *Chem. Rev.*, 2016, **116**, 10346–10413.

66 Y. Song, Y. Lv, M. Zhou, T.-Y. Luo, S. Zhao, N. L. Rosi, H. Yu, M. Zhu and R. Jin, Single-ligand exchange on an Au–Cu bimetal nanocluster and mechanism, *Nanoscale*, 2018, **10**, 12093–12099.

67 S. Hoseinkhani, R. Tubino, F. Meinardi and A. Monguzzi, Achieving the photon up-conversion thermodynamic yield upper limit by sensitized triplet–triplet annihilation, *Phys. Chem. Chem. Phys.*, 2015, **17**, 4020–4024.

68 J.-K. Li, M.-Y. Zhang, L. Zeng, L. Huang and X.-Y. Wang, NIR-Absorbing B,N-Heteroarene as Photosensitizer for High-

Performance NIR-to-Blue Triplet-Triplet Annihilation Upconversion, *Angew. Chem., Int. Ed.*, 2023, **62**, e202303093.
69 Y. Wei, Y. Wang, Q. Zhou, S. Zhang, B. Zhang, X. Zhou and S. Liu, Solvent effects on triplet–triplet annihilation upconversion kinetics of perylene with a Bodipy-phenyl-C_{60} photosensitizer, *Phys. Chem. Chem. Phys.*, 2020, **22**, 26372–26382.
70 K. Kumar Jha, A. Prabhakaran, R. Cane Sia, R. A. Arellano Reyes, N. Kumar Sarangi, T. Yang, K. Kumar, S. Kupfer, J. Guthmuller, T. E. Keyes and B. Dietzek-Ivanšić, Triplet Formation and Triplet-Triplet Annihilation Upconversion in Iodine Substituted Non-Orthogonal BODIPY-Perylene Dyads, *ChemPhotoChem*, 2023, **7**, e202300073.
71 M. Mitsui, D. Arima, Y. Kobayashi, E. Lee and Y. Niihori, On the Origin of Photoluminescence Enhancement in Biicosahedral $AgAu_{25}-$ Nanoclusters (x = 0–13) and Their Application to Triplet–Triplet Annihilation Photon Upconversion, *Adv. Opt. Mater.*, 2022, **10**, 2200864.
72 S. Medina Rivero, M. J. Alonso-Navarro, C. Tonnelé, J. M. Marín-Beloqui, F. Suárez-Blas, T. M. Clarke, S. Kang, J. Oh, M. M. Ramos, D. Kim, D. Casanova, J. L. Segura and J. Casado, V-Shaped Tröger Oligothiophenes Boost Triplet Formation by CT Mediation and Symmetry Breaking, *J. Am. Chem. Soc.*, 2023, **145**, 27295–27306.
73 P. Bharmoria, H. Bildirir and K. Moth-Poulsen, Triplet–triplet annihilation based near infrared to visible molecular photon upconversion, *Chem. Soc. Rev.*, 2020, **49**, 6529–6554.
74 Y. Niihori, T. Kosaka and Y. Negishi, Triplet–triplet annihilation-based photon upconversion using nanoparticles and nanoclusters, *Mater. Horiz.*, 2024, **11**, 2304–2322.
75 C. Ye, V. Gray, J. Mårtensson and K. Börjesson, Annihilation *Versus* Excimer Formation by the Triplet Pair in Triplet–Triplet Annihilation Photon Upconversion, *J. Am. Chem. Soc.*, 2019, **141**, 9578–9584.
76 H. Chen, I. Roy, M. S. Myong, J. S. W. Seale, K. Cai, Y. Jiao, W. Liu, B. Song, L. Zhang, X. Zhao, Y. Feng, F. Liu, R. M. Young, M. R. Wasielewski and J. F. Stoddart, Triplet–Triplet Annihilation Upconversion in a Porphyrinic Molecular Container, *J. Am. Chem. Soc.*, 2023, **145**, 10061–10070.
77 Q. Li, J. Chai, S. Yang, Y. Song, T. Chen, C. Chen, H. Zhang, H. Yu and M. Zhu, Multiple Ways Realizing Charge-State Transform in Au-Cu Bimetallic Nanoclusters with Atomic Precision, *Small*, 2021, **17**, 1907114.
78 X. Kang, X. Wei, S. Jin, Q. Yuan, X. Luan, Y. Pei, S. Wang, M. Zhu and R. Jin, Rational construction of a library of M_{29} nanoclusters from monometallic to tetrametallic, *Proc. Natl. Acad. Sci. U. S. A.*, 2019, **116**, 18834–18840.
79 G. Bottari, G. de la Torre, D. M. Guldi and T. Torres, Covalent and Noncovalent Phthalocyanine−Carbon Nanostructure Systems: Synthesis, Photoinduced Electron Transfer, and Application to Molecular Photovoltaics, *Chem. Rev.*, 2010, **110**, 6768–6816.
80 Y.-M. Lee, W. Nam and S. Fukuzumi, Redox catalysis *via* photoinduced electron transfer, *Chem. Sci.*, 2023, **14**, 4205–4218.
81 A. Hagfeldt, G. Boschloo, L. Sun, L. Kloo and H. Pettersson, Dye-Sensitized Solar Cells, *Chem. Rev.*, 2010, **110**, 6595–6663.
82 F. Strieth-Kalthoff and F. Glorius, Triplet Energy Transfer Photocatalysis: Unlocking the Next Level, *Chem*, 2020, **6**, 1888–1903.
83 X. Feng, Y. Pi, Y. Song, C. Brzezinski, Z. Xu, Z. Li and W. Lin, Metal–Organic Frameworks Significantly Enhance Photocatalytic Hydrogen Evolution and CO_2 Reduction with Earth-Abundant Copper Photosensitizers, *J. Am. Chem. Soc.*, 2020, **142**, 690–695.
84 S. Fukuzumi, K. Ohkubo and T. Suenobu, Long-Lived Charge Separation and Applications in Artificial Photosynthesis, *Acc. Chem. Res.*, 2014, **47**, 1455–1464.
85 R. Yanagi, T. Zhao, D. Solanki, Z. Pan and S. Hu, Charge Separation in Photocatalysts: Mechanisms, Physical Parameters, and Design Principles, *ACS Energy Lett.*, 2022, **7**, 432–452.